J. Earth Syst. Sci. (2021)130 1
https://doi.org/10.1007/s12040-020-01500-2

Interpretation of ship-track magnetic data near Narcondam and Barren Island volcanoes revisited

Indrajit G Roy

Spaceage Geoconsulting, 5 Bick Place, Banks, ACT 2906, Australia.
e-mail: spaceage.geocon@gmail.com

MS received 7 April 2020; revised 2 September 2020; accepted 17 September 2020

We interpret the legacy ship-track magnetic and bathymetric profile data to investigate the role of the lithospheric scale West Andaman Fault (WAF) in the dormant Narcondam and active Barren Island volcanoes. We use data-based automated interpretation of total magnetic intensity (TMI) profiles using a contact model in order to delineate geometrical and physical parameters of several faults including the WAF and then investigate its implications in recent volcanism at the Barren Island. Our data-based interpretation of TMI data requires transformation of it into the first order analytical signal and tilt angle, which in turn, requires estimation of the first order horizontal and vertical derivatives of TMI data. We ensure robust estimation of the first order horizontal and vertical derivatives using Savitzky–Golay derivative filter and Hilbert–Noda transformation, respectively. We have identified several anomaly segments of the TMI anomaly profiles and used data-based quantitative interpretation in each segments with a contact model. We then make a comprehensive interpretation using bathymetry, geological setup and the results from quantitative data-based interpretation of magnetic data, and ascertain possible role of the WAF in Barren Island volcanism.

Keywords. Narcondam; Barren Island; volcano; West Andaman Fault; magnetic data.

1. Introduction

The dormant Narcondam and active Barren Island volcanoes are two significant structures recognised as sub-aerial seamounts in the Andaman–Nicobar subduction system. However, for the sake of clarity in the following text, we address the dormant volcano of Narcondam as a seamount and the active volcano of Barren Island as volcano. The detailed geophysical investigations near these two locations are, unfortunately limited. There are only three east–west oriented ship-track geoscientific profiles, one near the Narcondam seamount and two near the Barren Island volcano. The transact near Narcondam was conducted during the year 1974–1975 by the Scripp Institute of Oceanography (SIO), La Jolla, California (Curray *et al.* 1982), and the transacts near Barren Island were conducted in the year 1993 by the Geological Survey of India (GSI) (Banerjee *et al.* 1998), approximately after 2 years from the day of volcanic eruption at Barren Island which was quiescent for more than 200 years. In those marine geoscientific transacts along with other measurements, the total magnetic intensity (TMI) and bathymetric measurements were carried out. The magnetic profiles situated at the north and south of Barren Island were interpreted by Banerjee *et al.* (1998) and Banerjee and Shaw (2001). However, to the authors knowledge, the ship-track magnetic profile near Narcondam has not been interpreted yet. Our objective is to investigate the subsurface architecture near

Published online: 01 February 2021

Narcondam seamount and also near the active Barren Island volcano using ship-track magnetic and bathymetric profiles.

The major motivation in studying this geologically significant zone arises from the fact firstly, that the Andaman–Nicobar subduction system is tectonically most active and complex in nature; in that two strike-slip faults, the West Andaman Fault (WAF) and Sagaing Fault (SF) play vital role not only in the formation of Burma microplate, but also in maintaining active tectonism resulting in large megathrust earthquakes (Curray 2005; Singh 2005). Secondly, the Barren Island volcano is a lone active volcano situated on the Burma microplate and belongs to Neogene inner Island Arc of the Andaman–Nicobar chains of islands (Shanker *et al.* 2001), while there is a chain of active volcanoes with the extended arc near the island Sumatra of Indonesia associated with the strike-slip Great Sumatra Fault (GSF) (Rodolfo 1969; Curray 2005).

We, therefore, focus our investigation whether the WAF has had any role on the active volcanism of Barren Island. We use gradient-based quantitative interpretation of TMI profiles, where we use a contact model to identify and interpret the geological structure, such as fault and the fracture zones. We use the first order analytical signal and tilt angle transformation of TMI data and a set of closed form formulas (presented in Appendix A) in conducting quantitative interpretation of magnetic data. We investigate using the parameters delineated from a geological contact model and supplementary information, such as bathymetry, geological data, tectonic elements and also the results of geoscientiific studies broadly around the tectonic zone the possible role of WAF in the Barren Island active volcanism.

2. Geodynamic and general geological settings

2.1 *Geodynamics*

We give a brief background of tectonic settings of Andaman–Nicobar subduction system (ANSS) at the outset. There has been a great deal of interests spanning over many decades regarding tectonism associated with India–Eurasia continental collision and subduction of the Indian Plate below Eurasian Plate. A review of such works up to the year 2004 with some historical and anecdotal accounts is given in Curray (2005). Geodynamically the ANSS, bounded approximately between 2°N at the southern end near the islands Nias and Simeulue of Indonesian Archipelago to 16°N near coast of Yangon Peninsula of Myanmar, is complex in nature. Complexity arises due to: (1) existence of simultaneous convergence dynamics by the Indian Plate and Burma Microplate (figure 1), while the latter is overriding former to the Sunda Plate (Guzman-Speziale and Ni 1996; Gahalaut and Gahalaut 2007; Hurukawa *et al.* 2012) and (2) the nature of oblique convergence resulting strain partitioning (Fitch 1972; Satyabala 2003; Nielsen *et al.* 2004; Martin *et al.* 2014).

The Andaman–Nicobar island-arc is situated on the Burma Microplate. The island-arc and backarc Central Andaman Basin (CAB), was formed ∼3–4 Ma (Kamesh Raju *et al.* 2004; Curray 2005). However, the tectonic history of the subduction system is ∼59 Ma old when the Indian Plate collided with Eurasian (Southeast Asia) Plate and started rotating anticlockwise. But the anticlockwise rotation ceased around ∼55 Ma and convergence continued with a clockwise motion until the Indian Plate fully collided with the Eurasian Plate during Cenozoic Era (∼44 Ma) (Klootwijk *et al.* 1992; Curray 2005; Singh and Moeremans 2017). The coupled motion, such as rotation with translation during convergence resulted into a situation of oblique convergence, which in turn caused development of the strike-slip sliver faults, viz., the West Andaman Fault (WAF) and the Sagaing Fault (SF) along with a backarc extensional basin, the Andaman Sea (Peltzer and Tapponier 1998; McCaffrey 1992, 2009). Tankard *et al.* (1998) suggest that the oblique convergence and generation of the sliver faults WAF and SF were not exactly coeval with the clockwise rotation of Indian Plate rather the WAF and SF were formed around the middle to late Eocene (∼44 Ma), by that time clockwise motion had already started. In this complex tectonics regime, several plates or platelet, such as Indian, Eurasian, Australia, Sunda plates and Burma microplate have been contributing to the cause, making the region tectonically most active. We, however, focus only on the tectonic setup of the Indian Plate and Burma Microplate with respect to the Sunda Plate while studying NC seamount and BI volcano.

A major feature of convergence tectonics between the Indian and Sunda plates is the Sunda–Andaman Trench (SAT), a convergent boundary between these two plates where the Indian Plate subsides

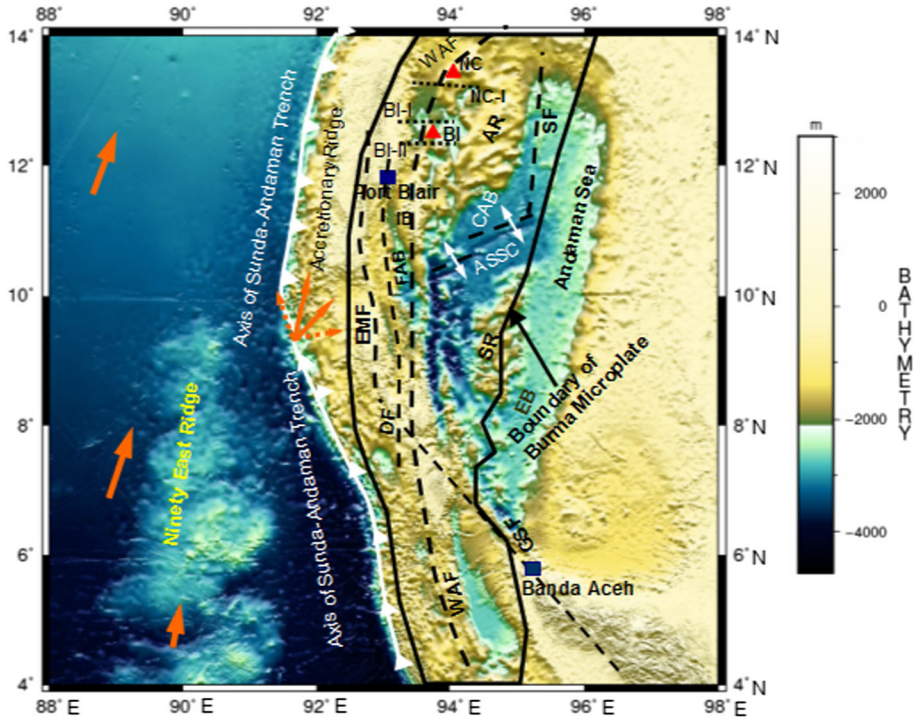

Figure 1. Geodynamic setting with tectonic elements of Andaman–Nicobar subduction system plotted on the bathymetry map of GEBCO. Axis of Sunda–Andaman Trench (▶ , white colour), boundary of Burma Microplate (—, black colour), WAF: West Andaman Fault (– –, black colour), GSF: Great Sumtra Fault (– –, black colour), SF: Sagaing Fault (– –, black colour), EMF: Eastern Margin Fault (– –, black colour), DF: Dilligent Fault (– –, black colour), EB: Eastern Basin, SR: Sewell Rises, AR: Alcock Rises, NC: Narcondam (▲, red colour), BI: Barren Island (▲, red colour), CAB: Central Andaman Basin, ASSC: Andaman Sea Spreading Centre (‡−‡, white colour), FAB: Fore-arc Basin, IB: Invisible Bank. Other features include Ninety East Ridge, Orange coloured arrows are the velocity vectors of plate motion, Andaman Sea, geophysical transacts NC-I, BI-I, BI-II (· · ·, black colour).

below the Sunda Plate forming Andaman–Nicobar island arc with an accretionary prism (identified as Andaman–Nicobar Ridge), Forearc Basin (FAB), Invisible Bank (IB), Central Andaman Basin (CAB), Andaman Sea Spreading Centre (ASSC), Alcock Rises (AR), Sewell Rises (SR), East Basin (EB) (figure 1). Altogether it is identified as the Andaman–Nicobar subduction system (ANSS). In a recent publication, Singh and Moeremans (2017) gave an anatomical detail of the ANSS. They emphasized using marine seismic data that the ANSS is characterized with shallow structures starting from SAT, where the Indian Plate is subducting below Sunda Plate up to the ASSC. The structures, such as Eastern Margin Fault (EMF), Diligent Fault (DF), seamount (NC) and an active volcano (BI) in addition to accretionary prism, FAB and IB are associated with the forearc and backarc subsystems due to the collisional tectonics between India and Sunda plates.

However, the most important outcomes of the convergent tectonics that exist between India and Eurasia, India-Australia with the Sunda Plate is the formation of Burma Microplate, a sliver region bounded between the forearc and backarc of the ANSS (Fitch 1972; McCaffrey 1992; Guzman-Speziale and Ni 1996; Stein and Okal 2005). Several workers, such as Fitch (1972), McCaffrey (1992) and Curray (2005) suggest that strain partitioning that arises due to oblique convergence of the India Plate was the major source in generating large lithospheric scale strike-slip faults, viz., (1) the SF which is starting at ∼26°N, near the Eastern Himalayan Syntaxis, the north-east corner point of collision between India and Eurasia plates, bisects Myanmar north-south and terminates at the ASSC and (2) the WAF which started at (∼14°N) is running subparallel to SAT up to ∼5°N reaches at the western margin of northern Sumatra. Further south, it ultimately becomes part of the Mentawai Fault Zone (MFZ) (not shown in figure 1). The WAF joins the Great Sumatran Fault (GSF) at 7°N near the Great Nicobar Island. On the other hand, the SF and WAF joins via Andaman Sea-ridge transform fault system near (10.25°N, 93.67°E) at the ASSC. Note that, the SF, WAF

and GSF are essentially strike slip faults although their convergence dynamics vary substantially.

The dynamics of oblique convergence can be envisaged through slip vectors which can be split into two components (figure 1), one perpendicular to the SAT and and the other parallel to it (Curray 2005). The magnitude of slip along the right lateral SF is 18 mm/a (Bertrand *et al.* 1998; Vigny *et al.* 2003). The GSF is also a right lateral strike-slip fault which has variable slips, such as 25 mm/a at the north-west and 10–20 mm/a at the south-east of Sumatra (Genrich *et al.* 2000). The WAF, on the other hand, demonstrates mixed type motion. For example, near the Andaman–Nicobar sector the WAF demonstrates predominantly strike-slip but at the southern end, almost near the tip of Sumatra it demonstrates along with strike-slip a thrust type motion (Singh 2005; Kamesh Raju *et al.* 2007).

2.2 *General geology*

The NC sub-aerial seamount, a crater-less dormant volcano is situated 70 km south of the shelf of Irrawaddy Delta. The peak of the seamount is 710 m above mean sea level and its circular base is at a depth of 2 km from the sea surface (Rodolfo 1969). Recent Ar^{40}/Ar^{39} dating of andesitic lava from NC yielded ages 0.55–0.56 Ma (Streck *et al.* 2011), which suggests that nearly half a million years ago the NC was an active volcano. However, the age of the volcano which is now dormant was found to be 1.8 ± 0.3 Ma from Ar^{40}/Ar^{39} dating of xenocrysts. The major rock types in NC are porphyritic dacite, basaltic-andesite, andesite and rhyolite, and also possesses evidence of mixing of both the mantle and crustal materials (Pal *et al.* 2007; Streck *et al.* 2011; Bandopadhyay 2017). The abundance of hornblende phenocryst in the volcanic lava groundmass of the NC is an important characteristic.

The BI, an active sub-aerial volcano, is situated 135 km north-east of Port Blair is only ~ 3 km wide with its caldera ~ 2 km wide. The highest point of the volcano is around 353 m above mean sea level and its base is around 2.2 km below the ocean surface. Although many authors describe the BI volcano as an active strato-volcano, we consider it as an active composite volcano, according to the definition by Davidson and De Silva (2000), which is now widely acceptable. The volcano is believed to be active since the Late Pliocene (Chhibber 1934; Rodolfo 1969; Bandopadhyay 2017) and it has been erupting intermittently, sometimes paroxysmally. Recent volcanic eruption occurred between September 2018 to January 2019 (Global Volcanism Program 2019). The age of the volcano from geochronological results using Ar^{40}/Ar^{39} dating of plagioclase xenocryst derived from crustal rock is 1.6 ± 3 Ma (Ray *et al.* 2015), which is slightly younger than that of the NC. The rock types associated with the BI volcano are mostly basalt and basaltic andesite (Bandopadhyay 2017). Unlike the NC seamount, the volcanic lava in the BI volcano hardly contains hornblende phenocryst (Streck *et al.* 2011).

3. Materials and methods

3.1 *Ship-track magnetic and bathymetric data*

We used ship-track magnetic and bathymetric data along E–W profiles near the active BI volcano (long. 93.86°E, lat. 12.28°N) and also near the NC seamount (long. 94.27°E, lat. 13.45°N). Both lie adjacent to the WAF in its eastern margin. Therefore, the magnetic profiles across WAF provide an opportunity to study the role of WAF on volcanic activity at the BI volcano. The ship-track magnetic and bathymetric profiles data were collected from National Geophysical Data Center (NGDC) (https://www.ngdc.noaa.gov/) and by digitizing from the published source (Banerjee *et al.* 1998). We considered three magnetic profiles, two on the either sides but of close proximity of the BI volcano, and one near the NC seamount. All three profiles are east–west oriented, almost across the strike of WAF. For the sake of convenience, we tag those profiles BI-I for north, BI-II for south of the BI volcano and NC-I for south of the NC seamount.

Ship-track marine magnetic and bathymetric data acquisition protocol used by both the SIO and GSI was similar except that the navigational means used in two occasions were different. In the 1970s Transit Satellite Navigation, known as TRANSIT, was used for positioning, but from 1990s Global Positioning System (GPS) was used in the navigation. The accuracy in GPS based positioning for 1993 marine magnetic data was ± 50 m (Banerjee and Shaw 2001), whereas navigational accuracy in marine geophysical survey using TRANSIT was ~ 400 m (Stansell 1983). The total magnetic intensity (TMI) was measured using proton precession magnetometer with ± 1 nT

accuracy, while the single beam or echo sounder was used for bathymetry. The mean spatial sampling interval in 1974–1975 vintage along the track data is 1.1 ± 0.6 km considering 19 samples within 5° square grid (Sharman and Metzger 1992). In the SIO ship-track magnetic data, the measurements were carried out at every 5 min interval. On the other hand, the data recording in the 1990s was much faster (2 min time interval).

3.2 *Data processing*

To collect the ship-track TMI data near the BI volcano, we redrew parts of the TMI profiles of figure 2 from Banerjee *et al.* (1998) and digitized those profiles. In order to maintain the highest possible frequency content in the data set, we first piecewise interpolated the digitized data using Hermite spline interpolation and then resampled the interpolated data with a sampling frequency twice the average Nyquist frequency which was estimated from unevenly sampled digitized data. The digitized data whether available directly or freshly digitized were: (1) piecewise interpolated and (2) resampled with 600 m data interval. The sampling interval that we chose was based on the consideration of cruise speed (18 km/hr) and a time interval of 2 min for each recorded data, as normally followed (Buchanan *et al.* 1996). Note

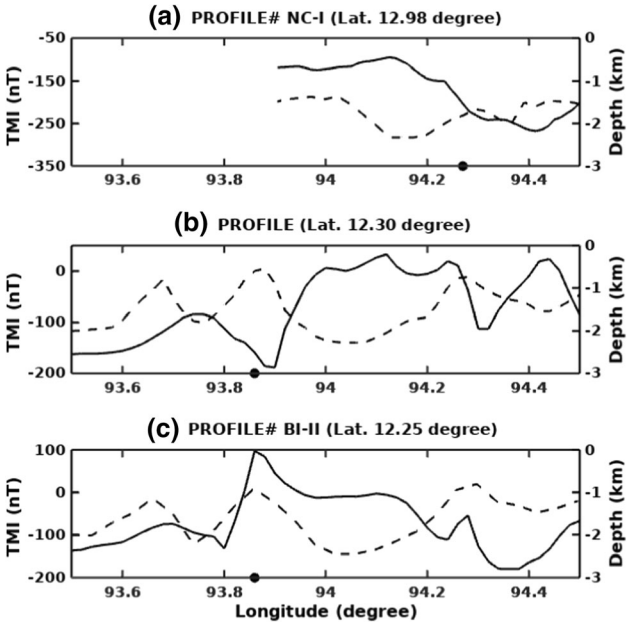

Figure 2. Magnetic and bathymetric profiles near Narcondam (NC-I) (panel a) and Barren Islands BI-I (panel b), BI-II (panel c). Bullet denotes nearest locations of Narcondam and BI volcanoes.

that the choice of sampling interval was in congruence with the spatial positioning accuracy which is at best 10% of the data interval. We then converted the profile data (both near the NC and BI volcanoes) from geodetic (longitude–latitude) coordinates frame defined over WGS84 ellipsoidal datum to UTM (easting–northing) coordinates frame. The three TMI and the associated bathymetric profiles are shown in panels (a–c) of figure 2. The bathymetric and TMI profiles are plotted in the same panel for the sake of comparison and qualitative interpretation.

Since the available magnetic data are from two different vintages with a time gap of nearly two decades, the major magnetic elements, such as declination (D), inclination (I) and magnetic field intensity (F) according to the IGRF model corresponding to the year 1975 and 1990 would be substantially different (table 1). As a part of data processing steps, we got an *a priori* estimate of the contaminated noise in data considering that the noise characteristic is significantly Gaussian random in nature. We used the method of median filtering to estimate noise in data as suggested in Roy (2018a). The procedure, however, provides only a rough estimate of the presence of random noise in data. We observed that the estimated noise for all three magnetic profiles was around 1.5%. The relatively small noise standard deviation, as estimated, was due to the process of piecewise interpolation and resampling, as mentioned above, which brought certain amount of smoothness in the digitized data set. The noise estimate was used in designing Savitzky–Golay derivative filter (Roy 2020) which in turn, was used in estimating the first order horizontal gradient of TMI data in a robust manner. The vertical gradient was then estimated using Hilbert transform of the first order horizontal gradient using Hilbert–Noda transformation matrix (Roy 2018b). Both the horizontal and vertical gradients are used in estimating the first order analytical signal and tilt angle transformation of TMI data. Those transformations were used in estimating parameters of a contact model.

4. Results and discussions

Careful observation on three magnetic and three bathymetric profiles (vide panels (a–c) of figure 2), one near the NC seamount (lat. 12.94°N) and the other two, one at lat. 12.30°N and another at lat.

Table 1. *Magnetic elements from IGRF 1975 and 1990.*

Profile	Latitude (°)	Longitude (°)	Declination (°)	Inclination (°)	Total field (nT)
Narcondam#1	12.98	94.0	−0.744	8.634	41,482
Barren#1	12.30	94.0	−1.062	8.542	41,520
Barren#2	12.25	94.0	−1.060	8.421	41,510

12.25°N near the active BI volcano provides the following first pass qualitative interpretation. (1) There are no one-to-one correlation between bathymetric and associated magnetic profiles, although visually it seems to have a similarity in the pattern of magnetic and bathymetric profiles near the NC seamount. The bathymetric profile suggests an upliftment of basement near the NC seamount. On the other hand, the part of magnetic profile situated at the west of the NC seamount demonstrates a typical reverse 'S' pattern suggesting the presence of geological contact with significant variation of magnetization in the basement. (2) The bathymetric profiles on either side of the Barren Island volcano are remarkably similar. The typical shape of ocean bottom topography in a near proximity to the volcano characterizes the type of volcano as a composite one which normally occurs in a convergent margin (Davidson and De Silva 2000). (3) The magnetic profiles at the north and south of BI volcano are distinctly different, although those two profiles exhibit similar pattern at the west of the volcano. Most importantly, the northern profile demonstrates a distinct magnetic low near the volcano whereas the southern profile demonstrates a magnetic low followed by a sharp magnetic high near the volcano, indicating distinct difference in magnetization in the basement. However, the overall pattern of magnetic profiles at the east of volcano remain more or less similar, except between the long. 94.3°E and 94.5°E, where the northern profile demonstrates a magnetic high but the southern profile demonstrates magnetic low, suggesting distinct variation of magnetization in basement from south of the volcano to the north.

Interestingly, the overall patterns of magnetic anomalies exhibited in both the magnetic profiles (north and south of the BI volcano extending from long. 93.5° to 93.8°E are more or less similar. This suggests that there is a similarity in gross architectural setting in the subsurface along the eastern part of those profiles, except that the structures formed due to recent volcanism are more proximal to one profile than the other. Clearly, the nature of magnetic profiles both for the west and east of Barren Island volcano are distinctly different. This is also the case for the magnetic profile near Narcondam seamount. In order to build up a databased quantitative interpretation of the entire magnetic profile using a contact model, we first divided each magnetic profile (at NC-I, BI-I and BI-II) into separate contiguous pieces, so that each piece of magnetic anomaly would adequately describe response of an isolated contact model. With careful observations from all three original magnetic profiles, we identified four segments in each selected portion of a magnetic anomaly profile, so that each segment could adequately represent anomaly response due to an isolated source of a contact model. For the sake of clarity, we present those segmented portions from each profile in different panels (appropriately tagged) in the same figure 3. We conducted databased quantitative interpretation after transforming each profile segment into the first order analytical signal and tilt angle domain and using formulas presented in Appendix A. We present the results of estimated model parameters corresponding to each segment in table 2.

4.1 *Profile NC-I*

Our first step, using the results of databased quantitative interpretation, was to identify the WAF and delineate its structural and physical attributes, such as the location of the trace of contact, depth of burial, dipping angle and magnetization. We actually conducted quantitative analysis separately for four anomaly segments, such as NC-I.1, NC-I.2, NC-I.3 and NC-I.4, respectively. The results are presented in table 2. We discuss quantitative analysis of the segments NC-I.1 and NC-I.2 first and next we discuss NC-I.3 and NC-I.4. We used following steps in identifying the WAF. Firstly, we consider its estimated location which correlates closely with the well established results of the other workers as cited in the text. For example, the NC seamount (which is a dormant volcano) is situated east of the WAF at a

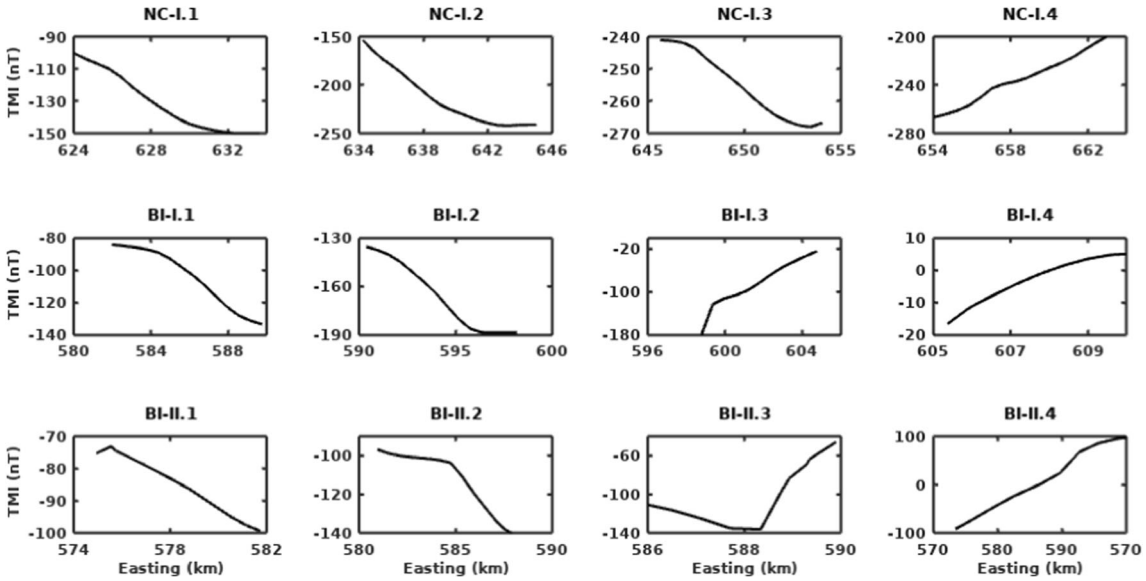

Figure 3. Plots of selected segments of magnetic profiles NC-I, BI-I and BI-II. Top row corresponds to four segments from NC-I, middle row from BI-I and bottom row from BI-II, respectively.

Table 2. *Results of segmented profile sections.*

Segments	ξ (km)	h (km)	θ (degree)	J_t (A/m)
NC-I.1	626.92	3.39	98.81	−11.05
NC-I.2	637.08	2.85	98.65	−11.64
NC-I.3	649.80	2.76	87.08	−5.43
NC-I.4	662.32	3.33	110.47	8.80
BI-I.1	586.26	2.63	94.50	−7.05
BI-I.2	593.90	2.66	90.47	−11.02
BI-I.3	601.15	2.03	89.98	9.34
BI-I.4	606.54	1.38	71.98	2.25
BI-II.1	576.80	3.75	114.85	−6.82
BI-II.2	586.09	1.33	88.97	−3.78
BI-II.3	588.75	0.79(?)	72.15	7.70
BI-II.4	592.30	1.74	103.08	28.99

location (lat. 13.45°N, long. 94.27°E). Therefore, the location of the WAF (lat. 12.98°N, long. 94.17°E), as estimated from the segment of magnetic profile NC-I.1, is considered most likely, which is ∼10 km west from the central location of seamount. The estimated depth of burial of the WAF near NC from the ocean surface is 3.39 km, suggesting that the WAF is buried ∼1 km below the ocean floor. The dipping angle of the fault (98.81°) suggests that the WAF is sub-vertical and reverse. Interestingly, the fault is attributed with a sharp negative magnetization contrasts −11 A/m, which indicates that the WAF is a boundary between two magnetically distinct regions, where the region in the west of the fault is strongly magnetized compared to that of the east of the fault. The magnetic segment NC-I.2 corresponds possibly to another fault (or a fracture) which lies (long. 94.26°E) in a close proximity of the NC seamount at a depth of ∼1 km with a dipping angle 98.65°, suggesting the fault is parallel to the WAF. The location of the trace of the fault indicates its association with the major lava vent of the once active volcano. The large negative magnetization contrast (−11.6 A/m), suggesting a strong demagnetization effect of the medium at the foot wall side of the fault (or contact) possibly due to volcanic activity, which was prominent nearly half a million years ago. It is also important to note that the variation of depth of the sea floor in those two fault locations is ∼460 m; in that the latter one corresponding to the anomaly segment NC-I.2 is shallower which could be inferred with a basement high.

The quantitative results corresponding to the anomaly segments NC-I.3 and NC-I.4 suggest that the former is associated with a nearly vertical fault, while the latter corresponds to a reverse one. The locations of these two faults along the transact are at longitude 94.36°E and 94.49°E, respectively. The former is dipping nearly vertical and is situated at a depth ∼1 km below ocean bottom. The latter one is near the margin of the Alcock Rises and at a depth ∼1.8 km below the ocean floor. The dipping angle of the fault (110.47°) suggests the nature of the fault as reverse. The strong positive magnetization contrast (8 A/m) is in conformity with basement upliftment as Alcock Rises. Note

that it is commonly perceived that the vertical upliftment of the crust could be attributed to serpentinization reactions that occur in the upper mantle peridotite (Zonenshain *et al.* 1989). It is important to note that the recent studies by Klein *et al.* (2013) demonstrate that the strong magnetization at a high temperature (∼400°C) near the convergent margin at the Mid Atlantic Ridge (MAR), as observed, was due to the abundance of magnetite mineral which was formed via serpentinization reactions.

4.2 *Profile BI-I*

We next discuss data-based quantitative interpretation of magnetic profile BI-I, which is situated at the North of Barren Island with an offset of ∼2 km. Like earlier occasion, as we did with NC-I magnetic profile, we divided the magnetic anomaly profile of BI-I into four segments, such as BI-I.1, BI-I.2, BI-I.3 and BI-I.4, respectively, and conducted quantitative analysis in each segment separately. The results are presented in table 2. We delineated the geometrical and physical parameters of WAF; in that we considered the anomaly segment BI-I.1 as an appropriate candidate in delineating the WAF. The location of WAF is estimated as (lat. 12.30°N, long. 93.79°E), which is ∼7.26 km west from the central location of the volcano. The estimated dipping angle (94.5°) suggests that the WAF is sub-vertical and reverse, and it is buried at a depth of ∼1.1 km from the ocean floor. The WAF is associated with a strong negative magnetization contrast (−7 A/m), as also observed with the profile NC-I, but in this occasion it is with a lesser magnitude. The location of the fault corresponding to the magnetic anomaly segment BI-I.2 is estimated as (lat. 12.30°N, long. 93.86°E), which is coinciding with the central location of the BI volcano. The dipping angle (90.47°) suggests the vertical nature of the fault separating two media with a strong negative magnetization contrast (∼−11 A/m). The depth of burial of the fault is ∼2 km from the ocean floor, whereas the depth of the ocean floor is ∼0.62 km. The results suggest that the fault is associated with a fracture, possibly the volcanic vent.

There are two more fault structures associated with the anomaly segments BI-I.3 and BI-I.4 which are located at (lat. 12.30°N, long. 93.93°E) and (lat. 12.30°N, long. 93.98°E), or ∼7.6 and 13 km farther east from the central location of the volcano, respectively. The former is dipping vertically and is buried at a depth ∼1 km below the ocean floor. On the other hand, the latter is dipping forward with an angle 71° and is buried at a depth ∼0.6 km below the ocean floor. But most importantly, the magnetization contrast for the fault BI-I.3 is strongly positive (9 A/m) and for the fault BI-I.4 is positive but is having lower magnetic magnitude (2 A/m).

4.3 *Profile BI-II*

The BI-II magnetic profile which is situated at the south of BI volcano with an offset of ∼5.5 km differs from that of the BI-I magnetic profile, especially the portion of the magnetic profile just east of the central location of the volcano. For the purpose of quantitative interpretation, we divided the profile into four segments BI-II.1, BI-II.2, BI-II.3 and BI-II.4, respectively, and interpreted each segment separately. The fault associated with the BI-II.1 magnetic anomaly is identified as the WAF, which is situated at (lat. 12.25°N, long. 93.71°E) ∼16.7 km from the central location of the volcano. With an offset of ∼7.7 km such a large movement (∼9.5 km) suggests possible rotation, a transpressional expression of the WAF. Note that Martin *et al.* (2014) reported 10–15 km wide transpressional faulting of the WAF at the edge of Aceh Basin of Sumatra. The dipping angle of the fault is 114°, suggesting a reverse faulting and the fault is characterized with the negative magnetization contrast (−6.83 A/m). The fault associated with the magnetic anomaly profile BI-II.2 is located at (lat. 12.25°N, long. 93.79°E), ∼7.5 km west of the central location of the volcano. The fault is steeply dipping (88.97°) and is buried shallow (∼160 m) below the ocean floor. The fault is also associated with negative magnetization contrast (−3.78 A/m). This is possibly the secondary fracture associated with the WAF.

The other two fault structures associated with the anomaly segments BI-II.3 and BI-II.4 are located at (lat. 12.25°N, long. 93.81°E) and (lat. 12.25°N, long. 93.85°E), respectively. Or in other words, the fault associated with the anomaly segment BI-II.3 is situated nearly 4 km from the volcano, but the fault associated with the anomaly segment BI-II.4 is almost nearly at the central location of the volcano. The former is dipping (72.15°) with an acute angle, suggesting the normal whereas the latter is dipping (103.08°) with an

obtuse angle suggesting reverse faulting. The depth of burial of the fault associated with BI-II.3 is somewhat underestimated and hence, we constrained it with the depth to the ocean floor. The depth of burial of the fault associated with the anomaly segment BI-II.4 is ∼700 m from the ocean floor. Both the faults are characterized with strong positive magnetization contrasts, such as 7.70 and 29 A/m, respectively.

4.4 *Implications of WAF in BI volcanism*

The WAF which is also identified as Invisible Bank Fault (IBF) (Curray 2005) is located almost at easternmost edge of Invisible Bank (IB), an uplifted structure comprised mainly of intrusive volcanics (Roy and Chopra 1987; Curray 2005). Curray (2005) interpreted that the reverse faulting and the compressional regime due to seafloor spreading is the major cause of IB structure as a post-Miocene uplift. The current results on the WAF, as demonstrated above, is commensurate with the interpretation of Curray (2005). It is important to note that the WAF is consistently characterized with strong negative magnetization contrast, suggesting the intrusive volcanics associated with IB is magnetically stronger than the oceanic crust. The major rock type of the oceanic crust associated with a convergent margin is mid ocean ridge basalt (MORB) (Smith 1990; Shau *et al.* 2004). The major magnetic carrier of such type of basalt is the mineral titanomeghamite, which forms due to low temperature oxidation (Ade-Hall *et al.* 1971; Johnson and Merril 1973; Kent and Gee 1994). The MORB type basalt, as observed in samples from Southeast Indian Ocean during Ocean Drilling program Leg 187, demonstrates in possessing very low coercivity remanence which causes decrease in normal remanent magnetization (NRM) with the increase of crust age (Shau *et al.* 2004). The average NRM, as reported in Shau *et al.* (2004), ranges from 1.16 to 8.71 A/m. The Curie temperature of MORB-type basalt with younger in age ranges from 100° to 240°C (Kent and Gee 1994), the range may increase up to 400°C for older aged basalt (Shau *et al.* 2004). The values of magnetization as estimated for the WAF in all three magnetic profiles are in agreement with the reported values as discussed.

The possible role of the WAF in BI volcanism are the following: (1) facilitating for hydration of the mantle rock by providing a passage of seawater to enter into and (2) generating horizontal compressional force in order to generate tensile crack facilitating the magma ascension. Those two conditions are associated with the generation of magma and its transport. To satisfy the first condition, it requires a large lithospheric scale fault or fracture, which would act as a conduit and allow hydration of the upper mantle peridotite to lower the solidus point in order to become the potential magma reservoir. Recently, Sarafian *et al.* (2017) demonstrate that the hydration of peridotite (with 140 µg/g H_2O) at 1.5 GPa pressure causes lowering of its melting point from 1380° to 1320°C. Actually the oceanic mantle at a convergent or divergent boundary contains ∼5 times more water (660 µg/g H_2O) (Shimizu *et al.* 2016) which results in further lowering of the temperature for the solidus. The WAF evidently satisfies the first condition, as the WAF is a lithospheric scale fault.

The composite volcano, such as BI volcano, is characterized with a magma chamber (or reservoir) which is essentially a sill type intrusive structure in the lower crust, and the magma chamber is being continuously fed by dikes injected from the upper mantle (Menand *et al.* 2010; Gudmundsson 2012). But a sill type intrusion in a lower crust requires horizontal stratification forming a weak plane, about which our idea still remains limited. However, Taisne and Jaupart (2009) demonstrated through numerical modelling that sill intrusion within a crust requires at least 700 m thick low-density stratigraphy layer which could be 2 km thick on an average. Recently, a direct evidence of intrusive volcanic sill at a depth 17.5–22 km in the lower crust at northern North Sea has been demonstrated through 3D seismic image using broad band seismic data (Wrona *et al.* 2019). The magma chamber in a molten state, once formed, rests in a lithostatic equilibrium within the host rock in absence of any unrest. An initiation of hydrofracturing or faulting occur when an excess pressure builds up in the magma chamber. Horizontal compression due to tectonic stress build up is one of the major causes of excess pressure within a magma chamber that initiates tensile crack and facilitates magma ascent (Gudmundsson 2012). We have discussed in the above using quantitative interpretation of BI-I and BI-II magnetic profiles that the WAF has a transpressional expression which indicates a compressional stress regime within the crust facilitating magma ascent in the volcano. Using quantitative interpretation of ship-track magnetic and bathymetric profiles and also

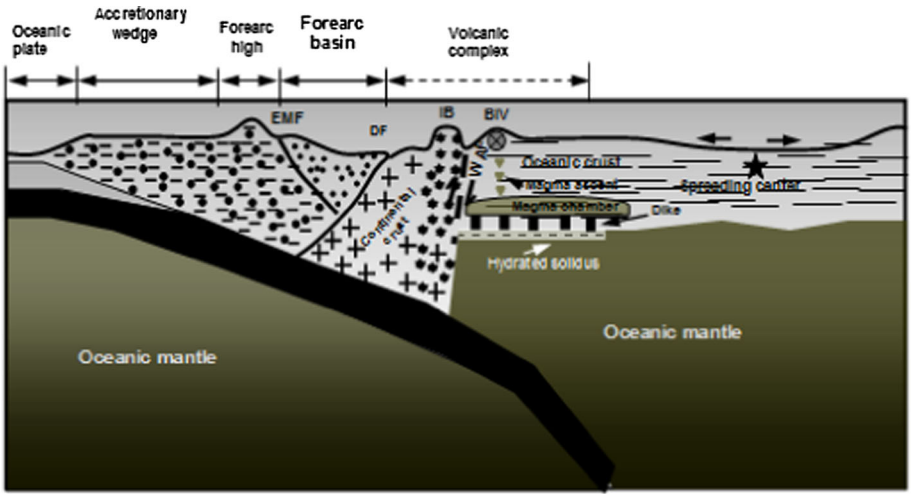

Figure 4. Schematic plot of vertical geological section along a E–W oriented transact near Barren Island (BI) volcano.

using available data from the published literature, we prepare a schematic representation subsurface structures (figure 4) along east–west transaction near Barren Island volcano.

5. Conclusion

We conduct data-based interpretation of ship-track magnetic profile data near dormant Narcondam and active Barren Island volcanoes. These two volcanoes are located near the large lithopheric scale the West Andaman Fault. We conducted data-based quantitative interpretation via the first order analytical signal and tilt angle transformation of total magnetic intensity data using a dipping contact model to identify and parametrize the West Andaman Fault and explained its role in both the Narcondam and Barren Island volcanoes. We have identified transpression expression of the WAF near BI volcano and have concluded that the horizontal stress built-up due to active tectonism is the possible cause of active volcanism. We also discuss about the possible cause of low magnetization at the foot wall side of the WAF near the dormant Narcondam and active Barren Island volcanoes and also the sharp magnetic high near the active Barren Island volcano.

Acknowledgements

The author would like to thank both the anonymous reviewers for their illuminated reviews which help in improving the manuscript substantially. The current research is supported by Spaceage Geoconsulting, a research oriented consulting firm.

Appendix A: Formulation

The horizontal and vertical gradients of the measured TMI response on the datum surface due to a buried contact model (figure A1), according to (Nabighian 1972; Roy 2013), are given as:

$$T_x(x) = 2\,\kappa\,F\eta\,\sin\theta\,\frac{h\cos\phi + (x - x_c)\sin\phi}{h^2 + (x - x_c)^2}, \tag{A1}$$

$$T_z(x) = 2\,\kappa\,F\eta\,\sin\theta\,\frac{(x - x_c)\cos\phi - h\sin\phi}{h^2 + (x - x_c)^2}, \tag{A2}$$

where T_x and T_z are the horizontal and vertical gradients, x_c is the horizontal location of the contact from the origin, κ is magnetic susceptibility contrast measured in SI unit, F is the geomagnetic field intensity, measured in nT. The product of magnetic susceptibility contrast κ and the field intensity F can be replaced with the magnetization J_t, where is the total magnetization due to induced and remanent magnetization of the oceanic crust. It then turns out as

$$T_x(x) = 2\,J_t\eta\,\sin\theta\,\frac{h\cos\phi + (x - x_c)\sin\phi}{h^2 + (x - x_c)^2}, \tag{A3}$$

$$T_z(x) = 2\,J_t\eta\,\sin\theta\,\frac{(x - x_c)\cos\phi - h\sin\phi}{h^2 + (x - x_c)^2}, \tag{A4}$$

with

$$\eta = 1 - \cos^2 I \sin^2\alpha, \tag{A5}$$

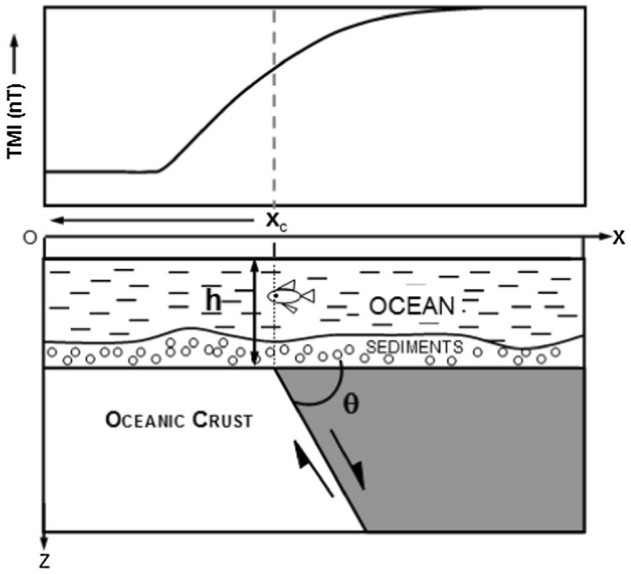

Figure A1. Schematic plot of a buried contact model and the total magnetic intensity (TMI) response.

$$\phi = 2\beta - \theta - 90^{\circ}, \tag{A6}$$

$$\tan\beta = \frac{\tan I}{\cos\alpha}, \tag{A7}$$

where I is the inclination of geomagnetic field at a place and α is the angle between magnetic north and the profile. From equation (A5), it can be said that $0 < \eta \leq 1$, where η takes on the maximum value 1 either at the geomagnetic pole or equator with $\alpha = 0$. Please note firstly that the magnetization is normally expressed in terms of A/m while the TMI anomaly is measured in terms of nT, the conversion factor from nT to A/m being $1\,\text{nT} = 0.7974 \times 10^{-3}$ A/m, and secondly the magnetization J_t used in the formulas imply magnetization contrast instead of magnetization of individual rock type. With the conversion, as mentioned, the unit for horizontal and vertical gradients becomes A/m^2. The close form formulae for the first order analytical signal and tilt angle are given as:

$$\mathcal{A}(x) = \frac{2\,J_t\,\eta\,\sin\theta}{\left[h^2 + (x - x_c)^2\right]^{1/2}}, \tag{A8}$$

and

$$\delta(x) = \arctan\left[\frac{(x - x_c)\cos\phi - h\sin\phi}{|(x - x_c)\sin\phi + h\cos\phi\,|}\right], \tag{A9}$$

where $|\cdot|$ denotes the absolute value ensuring that the denominator of equation (A9) remains positive valued so that the TA lies between -90° and 90°.

Clearly from equation (A8) one finds that the first order analytical signal would attain peak maximum at $x = x_c$. Following are the cases that hold.

Case 1: At the trace or edge of a contact, i.e., $x = x_c$

$$\mathcal{A}(x)\Big|_{x=x_c} = \frac{2\,J_t\,\eta\,\sin\theta}{h}. \tag{A10}$$

From equations (A8 and A10), it is clear that the response of the first order analytic signal is symmetric and it attains a peak at the trace of the contact. Further, from equations (A6 and A9) with a little algebraic manipulation we write

$$\delta(x)\Big|_{x=x_c} = 90^{\circ} + (\theta - 2\beta). \tag{A11}$$

Case 2: When TA attains zero value then using equations (A6 and A9), we write

$$x_c - x_0 = h\,\cot(\theta - 2\,\beta). \tag{A12}$$

where x_0 is the position corresponds to the zero value of the TA. Therefore, once x_c is determined from the position of the peak of $\mathcal{A}(x)$ response the dip of the contact θ can be determined using equations (A7 and A11), as the value of inclination I and azimuth α are known. Further, on delineating the position of zero value x_0 of TA the depth of burial of the contact can be easily determined and using equations (A7 and A12). The amplitude of magnetization J_t is readily determined from equation (A10) once all other parameters are either determined or known *a priori*.

Author statement

The principal author has contributed entirely in the paper that includes conceptualization, data processing, data modelling, interpretation and also preparation of the manuscript.

References

Ade-Hall J M, Palmer H C and Hubbard T P 1971 The magnetic and opaque petrological response of basalts to regional hydrothermal alteration; *Geophys. J. Roy. Astron. Soc.* **24** 137–174, https://doi.org/10.1111/j.1365-246X.1971.tb02171.x.

Bandopadhyay P C 2017 Inner-arc volcanism: Barren and Narcondam islands; Chapter 12, In: The Andaman-Nicobar Accretionary Ridge: Geology, Tectonics and Hazards (eds) Bandopadhyay P C and Carter A, *Memoirs Geol. Soc. London* **47** 167–192, https://doi.org/10.1144/M47.12.

Banerjee B and Shaw R K 2001 Marine magnetic anomalies near the Barren Island volcano, Andaman Sea; *Curr. Sci.* **81(7)** 816–818.

Banerjee B, Subba Rao P B V, Gupta G, Joseph E J and Singh B P 1998 Results from a magnetic survey and geomagnetic depth sounding in the pot-eruption phase of the Barren Island volcano; *Earth Planet. Space* **50** 327–338, https://doi.org/10.1186/BF03352119.

Bertrand G, Rangin C, Maury R C, Htun H M, Bellon H and Guillaud J-P 1998 The Singu basalts (Myanmar): New constraints for the amount of recent offset in Sagaing Fault; *C. R. Acad. Sci.* **327** 479–484, https://doi.org/10.1016/S1251-8050(99)80076-7.

Buchanan S K, Scutton R A, Edwards R A and Whitemarsh R B 1996 Marine magnetic data processing in equatorial regions off Ghana; *Geophys. J. Int.* **125** 123–131, https://doi.org/10.1111/j.1365-246X.1996.tb06539.x.

Chhibber H L 1934 *Geology of Burma*; MacMillan & Co., London, 530p.

Curray J R 2005 Tectonics and history of Andaman Sea region; *J. Asian Earth Sci.* **25** 187–228, https://doi.org/10.1016/j.jseaes.2004.09.001.

Curray J R, Emmel F J, Moore D G and Raitt R W 1982 Structure, tectonics and geological history of the northeastern Indian Ocean; In: *The Ocean Basins and Margins* (eds) Nairn A E M and Stehli F G, Springer, Boston, MA, pp. 399–450.

Davidson J and De Silva S 2000 Composite volcanoes; In: *Encyclopedia of Volcanoes* (eds) Sigurdsson H *et al.*, Academic Press, San Diego, pp. 663–681.

Fitch T J 1972 Plate convergence, transcurrent faults and internal deformation adjacent to south-east Asia and western Pacific; *J. Geophys. Res.* **77(23)** 4432–4460, https://doi.org/10.1029/JB077i023p04432.

Gahalaut V and Gahalaut K 2007 Burma Plate motion; *J. Geophys. Res.* **112** B10402, https://doi.org/10.1029/2007JB004928.

Genrich J F, Bock Y and McCaffrey R *et al.* 2000 Distribution of slip at the northern Sumatra fault system; *J. Geophys. Res.* **105(B12)** 28,327–28,341, https://doi.org/10.1029/2000JB900158.

Global Volcanism Program 2019 Report on Barren Island (India) *Bulletin of the global volcanism network* (eds) Krippner J B and Venzke E, Smithsonian Institution, **44(2)**, https://doi.org/10.5479/si.GVP.BGVN201902-260010.

Gudmundsson A 2012 Magma chambers: Formation, local stresses, excess pressure, and compartments; *J. Volcanol. Geotherm. Res.* **237–238** 19–41, https://doi.org/10.1016/j.jvolgeores.2012.05.015.

Guzman-Speziale M and Ni J F 1996 Seismicity and active tectonics of the western Sunda Arc; In: *The tectonic evolution of Asia* (eds) Yin A and Harrison T M, Cambridge University Press, New York, pp. 63–84.

Hurukawa N, Tun P P and Shibazaki B 2012 Detailed geometry of the subducting Indian Plate beneath the Burma Plate and subcrustal seismicity beneath in the Burma Plate derived from joint hypocenter relocation; *Earth Planet. Space* **64** 333–343, https://doi.org/10.5047/eps.2011.10.011.

Johnson H P and Merrill R T 1973 Low-temperature oxidation of a titanomagnetite and the implications for paleomagnetism; *J. Geophys. Res.* **78** 4938–4949, https://doi.org/10.1029/JB078i023p04938.

Kamesh Raju K A, Ramaprasad T, Rao P S, Rao B R and Varghese J 2004 New insights into the tectonic evolution of the Andaman basin, northeast Indian ocean; *Earth Planet. Sci. Lett.* **221** 145–162, https://doi.org/10.1016/S0012-821X(04)00075-5.

Kamesh Raju K A, Murty G P S, Amarnath D and Kumar M L M 2007 The West Andaman Fault and its influence on the aftershock pattern of the recent megathurst earthquakes in the Andaman–Sumatra region; *Geophys. Res. Lett.* **34(3)** L03305, https://doi.org/10.1029/2006GL028730.

Kent D V and Gee J 1994 Grain size-dependent alteration and magnetization of oceanic basalts; *Science* **265(5178)** 1561–1563, https://doi.org/10.1126/science.265.5178.1561.

Klein F, Bach W and McCollom T M 2013 Compositional controls on hydrogen generation during serpentinization of ultramafic rocks; *Lithos* **178** 55–69, https://doi.org/10.1016/j.lithos.2013.03.008.

Klootwijk C T, Gec J S, Peirce J W, Smith G M and McFadden P L 1992 An early India-Asia contact: Paleomagnetic constraints from Ninetyeast Ridge, ODP Leg 121; *Geology* **20** 395–398, https://doi.org/10.1130/0091-7613(1992)020<0395:AEIACP>2.3.CO;2.

Martin K M, Gulick S P S, Austin(Jr) J A, Berglar K, Franke D and Udrekh 2014 The West Andaman Fault: A complex strain-partitioning boundary at the seaward edge of the Aceh Basin, offshore Sumatra; *Tectonics* **33** 786–806, https://doi.org/10.1002/2013TC003475.

McCaffrey R 1992 Oblique plate convergence, slip vectors and forearc deformation; *J. Geophys. Res.* **97** 8905–8915, https://doi.org/10.1029/92JB00483.

McCaffrey R 2009 The tectonic framework of the Sumatra subduction zone; *Ann. Rev. Earth Planet. Sci.* **37** 345–366, https://doi.org/10.1146/annurev.earth.031208.100212.

Menand T, Daniels K A and Benghiat P 2010 Dyke propagation and sill formation in a compressive tectonic environment; *J. Geophys. Res.* **115** B08201, https://doi.org/10.1029/2009JB006791.

Nabighian M N 1972 The analytical signal of two-dimensional magnetic bodies with polygonal cross section: Its properties and use for automated anomaly interpretation; *Geophysics* **37** 507–517, https://doi.org/10.1190/1.1440276.

Nielsen C, Chamot-Rooke N and Rangin C *et al.* 2004 From partial to full strain partitioning along the Indo-Burmese hyperbolique subduction; *Mar. Geol.* **209** 303–327, https://doi.org/10.1016/j.margeo.2004.05.001.

Pal T, Mitra S K, Sengupta S, Katari A, Bandopadhyay P C and Bhattacharya A K 2007 Dacite-andesites of Narcondam volcano in the Andaman Sea – an imprint of magma mixing in the inner arc of the Andaman-Java subduction system; *J. Volcanol. Geotherm. Res.* **168** 93–113, https://doi.org/10.1016/j.jvolgeores.2007.08.005.

Peltzer G and Tapponier P 1988 Formation and evolution of strike-slip faults, rift and basins during India-Asia collisions: an experimental approach; *J. Geophys. Res.* **93** 15,085–15,097, https://doi.org/10.1029/JB093iB12p15085.

Ray J S, Pande K and Bhutani R 2015 Ar^{40}/Ar^{39} geochronology of subaerial lava flows of Barren Island volcano and the deep crust beneath the Andaman Island Arc, Burma Microplate; *Bull. Volcanol.* **77** 57, https://doi.org/10.1007/s00445-015-0944-9.

Rodolfo K S 1969 Bathymetry and marine geology of the Andaman Basin and tectonic implication for south-east

Asia; *Geol. Soc. Am. Bull.* **80** 1203–1230, https://doi.org/10.1130/0016-7606(1969)80[1203:BAMGOT]2.0.CO;2.

Roy I G 2013 Tilt angle interpretation of dipping fault model; *J. Appl. Geophys.* **98** 33–43, https://doi.org/10.1016/j.jappgeo.2013.07.009.

Roy I G 2018a On robust estimation of derivative of noisy dataset: Application on temperature gradient of ocean water column; *J. Indian Geophys. Union* **22(4)** 371–378.

Roy I G 2018b On the Hilbert-Noda transformation of geophysical time series; *Geophys. J. Int.* **215** 2198–2205, https://doi.org/10.1093/gji/ggy402.

Roy I G 2020 An optimal Savitzky–Golay derivative filter with geophysical applications: An example of self-potential data; *Geophys. Prospect.* **68(3)** 1041–1056, https://doi.org/10.1111/1365-2478.12892.

Roy T K and Chopra N N 1987 Wrench faulting in Andaman forearc basin, India; *Proc. Offshore Technol. Conf.* **19** 393–404.

Sarafian E, Gaetani G A, Hauri E H and Sarafian A R 2017 Experimental constraints on the damp peridotite solidus and oceanic mantle potential temperature; *Science* **355** 942–945, https://doi.org/10.1126/science.aaj2165.

Satyabala S P 2003 Oblique plate convergence in the Indo-Burma (Myanmar) subduction region; *Pure Appl. Geophys.* **160** 1611–1650, https://doi.org/10.1007/S00024-003-2378-0.

Shanker R, Haldar D, Absar A and Chakraborty S C 2001 Pictorial monograph of the Barren Island volcano: The lone active volcano in the Indian subcontinent; *Geol. Surv. India Spec. Publ.* **67** 87.

Sharman G F and Metzger D 1992 Marine magnetic data holdings of World Data Center A for marine geology and geophysics; In: *Types and characteristics data for geomagnetic field modelling* (eds) Langel R A and Baldwin R T, pp. 137–148.

Shau Y-H, Torii M, Horng C-S and Liang W-T 2004 Magnetic properties of mid-ocean-ridge basalts from Ocean Drilling Program Leg 187; In: Proceedings of Ocean Drilling Program, (eds) Pedersen R B, Christie D M and Miller D J, *Scientific Results* **186** 1–25.

Shimizu K, Saal A E, Myers C E, Nagel A N, Hauri E, Forsyth D, Kemenetsky V S and Niu Y 2016 Two component mantle melting mixing model for the generation of mid-ocean ridge basalt: Implications for the volatile content of the Pacific upper mantle; *Geochim. Cosmochim. Acta* **176** 44–80, https://doi.org/10.1016/j.gca.2015.10.033.

Singh S C 2005 Sumatra earthquake research indicates why rupture propagated northward; *EOS Trans. Am. Geophys. Union* **86(48)** 497–502, https://doi.org/10.1029/2005EO480002.

Singh S C and Moeremans R 2017 Anatomy of the Andaman–Nicobar subduction system from seismic reflection data; In: The Andaman-Nicobar accretionary ridge: geology, tectonics and hazards (eds) Bandopadhyay P C and Carter A, *Geol. Soc., London Memoir.* **47** 193–204, https://doi.org/10.1144/M47.13.

Smith G M 1990 The magnetic structure of the marine basement; *Rev. Aquat. Sci.* **2** 205-227.

Stansell T A 1983 *The Transit Navigation Satellite System: Status Theory Performance Applications*; Magnavox, https://www.ion.org/museum/files/TransitBooklet.pdf.

Stein S and Okal E A 2005 Speed and size of the Sumatra earthquake; *Nature* **434** 581–582, https://doi.org/10.1038/434581a.

Streck M J, Ramos F, Gillam A, Haldar D and Duncan R A 2011 The Intra-oceanic Barren Island and Narcondam Arc Volcanoes, Andaman Sea: implications for subduction input and crustal overprint of a depleted mantle source; Chapter 11, In: *Topics in Igneous Petrology* (eds) Ray J, Sen G and Ghosh B, Springer, Dordrecht, pp. 240–273, https://doi.org/10.1007/978-90-481-9600-5-11.

Taisne B and Jaupart C 2009 Dike propagation through layered rocks; *J. Geophys. Res.* **114** B09203, https://doi.org/10.1029/2008JB006228.

Tankard A J, Balkwil H R, Mehra A and Aung Din 1998 Tertiary wrench fault tectonics and sedimentation in the central basin of Burma; *Am. Assoc. Petrol. Geol. Bull.* **78** 1165 (abstract).

Vigny C, Socquet A, Rangin C, Chamot-Rooke M, Pubellier M, Bouin M N and Becker M 2003 Present-day crustal deformation at Sagaing Fault, Myanmar; *J. Geophys. Res.* **118** 3592–3609, https://doi.org/10.1029/2002JB001999.

Wrona T, Magee C, Fossen H, Gawthorpe R L, Bell R E, Jackson CA-L and Faleide J I 2019 3-D seismic images of an extensive igneous sill in the lower crust; *Geology* **47** 729–733, https://doi.org/10.1130/G46.150.1.

Zonenshain L P, Kuzmin M I, Lisitsin A P, Bogdanov Yu A and Baranov B V 1989 Tectonics of Mid Atlantic rift valley between the TAG and MARK areas (24–26°N): Evidence for vertical tectonism; *Tectonophys.* **159(1–2)** 1–23, https://doi.org/10.1016/0040-1951(89)90167-4.

Corresponding editor: N V Chalapathi Rao